Applied Surface Science Advances 26 (2025) 100718

Contents lists available at ScienceDirect

Applied Surface Science Advances

journal homepage: www.sciencedirect.com/journal/applied-surface-science-advances

Full Length Article

Localized creation of bubble domains in Fe_3GaTe_2 by conductive atomic force microscopy

Chak-Ming Liu [a,1], Yi-Jia Liu [a,1], Po-Chun Chang [b,c,1], Po-Wei Chen [a], Masahiro Haze [d], Ming-Hsien Hsu [a], Neleena Nair Gopakumar [a], Yishui Zhou [b], Yung-Hsiang Tung [b], Sabreen Hammouda [b], Chao-Hung Du [c], Yukio Hasegawa [d], Yixi Su [b], Hsiang-Chih Chiu [a,*], Wen-Chin Lin [a,*]

[a] Department of Physics, National Taiwan Normal University, Taipei 11677, Taiwan
[b] Jülich Centre for Neutron Science at Heinz Maier-Leibnitz-Zentrum, Forschungszentrum Jülich GmbH, Lichtenbergstr. 1, 85747 Garching, Germany
[c] Department of Physics, Tamkang University, New Taipei City 251301, Taiwan
[d] Institute for Solid State Physics, the University of Tokyo, 5-1-5, Kashiwa-no-ha, Kashiwa, Chiba 277-8581, Japan

ARTICLE INFO

Keywords:
Skyrmion
Magnetism
2D material
Conductive atomic force microscope
Magnetic force microscope
Scanning tunneling microscope

ABSTRACT

This study demonstrates the localized creation of bubble domains in the two-dimensional (2D) ferromagnetic material Fe_3GaTe_2 using conductive atomic force microscopy. By applying bias voltage to the tip under a perpendicular magnetic field, sufficient current is generated to induce localized Joule heating, transforming random stripe domains into bubble domains. The bubble domains were successfully induced under ambient conditions at room temperature and remained stable, as confirmed by magnetic force microscopy. For Fe_3GaTe_2 layers with thicknesses of 1 μm, 200 nm, and 100 nm, the average diameters of bubble domains were measured at 620 ± 100 nm, 325 ± 80 nm, and 230 ± 70 nm, respectively, approximately 20 % larger than the pristine stripe width. By optimizing parameters such as bias voltage, application duration, and tip temperature based on Fe_3GaTe_2 thickness, the induced bubble domain density could be precisely controlled, ranging from few bubble domains within areas < 5 μm^2 to nearly 10^4 bubble domains within 1200 μm^2. Furthermore, multi-point triggering demonstrated the re-writability of the domain structures, with non-overlapping domains remaining unaffected. These findings offer critical insights into the tunability of magnetic textures in 2D ferromagnets, providing a foundation for developing next-generation spintronic devices based on 2D heterostructures.

Introduction

In recent decades, two-dimensional (2D) van der Waals materials have garnered significant attention due to their diverse physical properties and potential applications in sub-nanometer-thick devices [1,2]. Notable examples include graphene, transition metal dichalcogenides (TMDs), and hexagonal boron nitride (h-BN) [1,3–5], which serve as a conductor, semiconductor, and insulator, respectively. However, the development of magnetic 2D materials with transition temperatures exceeding room temperature (RT) remains a major challenge [2,6]. Since 2016, research has demonstrated stable magnetic states in layered antiferromagnetic materials such as $NiPS_3$ and $FePS_3$ [2,6–8]. Despite their stability, these materials exhibit spin configurations that cancel out, limiting their practical use in spintronic devices. Subsequently, the discovery of intrinsic ferromagnetism in 2D materials, including CrI_3, $CrGeTe_3$, and Fe_3GeTe_2, marked a significant milestone [1,2,9,10]. Nevertheless, these materials face limitations such as complex interlayer coupling, significant reductions in Curie temperature (T_c), and susceptibility to oxidation or hydrolysis in ambient conditions. Thus, achieving ferromagnetic 2D materials with T_c above RT, strong perpendicular magnetic anisotropy (PMA), and high environmental stability remains a key objective.

In 2D-systems, such as thin films or multilayers, a uniform out-of-plane magnetization is often unstable due to dipolar magnetic coupling-induced shape anisotropy. To counteract this in-plane shape anisotropy, a strong PMA arising from spin-orbital coupling, symmetry

* Corresponding authors.
E-mail addresses: chiu@ntnu.edu.tw (H.-C. Chiu), wclin@ntnu.edu.tw (W.-C. Lin).
[1] The authors equally contributed to this work.

https://doi.org/10.1016/j.apsadv.2025.100718
Received 29 November 2024; Received in revised form 4 February 2025; Accepted 14 February 2025
Available online 22 February 2025

breaking, or other mechanisms is required. Recently, Fe_3GaTe_2, a 2D van der Waals material, has emerged as a promising candidate due to its exceptional magnetic properties [11–22]. Fe_3GaTe_2 exhibits robust PMA with a large saturation moment at RT and a T_c in the range of 350–380 K [11,12,16]. This stable ferromagnetism, combined with PMA, has enabled its application in various prototype spintronic devices, such as thermospin converters [19], nonlocal spin valves, and magnetic tunneling junctions [13–17]. Moreover, theoretical predictions by Ruiz et al. suggest that PMA and high T_c are maintained even in single-layer Fe_3GaTe_2 [12]. Strain engineering and electrostatic doping have been shown to effectively modulate its magnetism [12], and the reduction of interlayer spacing in thicker Fe_3GaTe_2 (~100 nm) enhances PMA significantly [23].

An especially exciting aspect of Fe_3GaTe_2 is its potential for hosting room-temperature-stabilized magnetic skyrmions (SKs)—nanoscale swirling spin textures with high potential for applications in memory and logic devices. Recent studies, such as those by Liu et al., have confirmed the material's capability to host SK bubbles [10,18,20,21,24,25]. Zhang et al.'s study reported that the sizes of stripe and SK bubbles strongly depend on the thickness of the magnetic 2D material, with their micromagnetic simulation results consistent with Kittel's law [22]. Consequently, the controlled creation, tuning, and manipulation of SKs in Fe_3GaTe_2 represent crucial and challenging areas of ongoing research [21,10,18,26–29]. In this study, we demonstrate a simple and effective method for the localized creation of bubble domains in the 2D magnetic material Fe_3GaTe_2, utilizing the Joule heating effect through a conductive atomic force microscope (cAFM) tip under a perpendicular magnetic field. We comprehensively investigate the influence of key parameters, including applied voltage, exposure duration, Fe_3GaTe_2 thickness, and tip temperature, and provide an in-depth discussion of their effects.

Experimental method

High-quality Fe_3GaTe_2 single crystals were synthesized using the chemical vapor transport (CVT) method. High-purity Fe granules, Ga lumps, and Te pieces were combined in a stoichiometric ratio of 3:1:2 and sealed in a vacuum quartz tube containing iodine (2 mg/cm^3) as a transport agent. To ensure material purity, all preparation steps were performed in a glove box. The sealed tube was then placed in a furnace with a temperature gradient of 760–710 °C for 7–10 days, followed by natural cooling to room temperature within the furnace. The crystalline structure was confirmed via X-ray diffraction (XRD) using a Bruker D2 PHASER diffractometer with Cu Kα radiation ($\lambda = 1.5406$ Å).

The collective magnetic properties of Fe_3GaTe_2 single crystals were investigated using a variable-temperature vibrating sample magnetometer (VT-VSM). Magnetic domain evolution was observed through a magneto-optical Kerr microscope (Evico Magnetics GmbH) in polar geometry [30,31]. Surface morphology and atomic structure were characterized with a low-temperature (6 K) ultra-high vacuum scanning tunneling microscope (LT-UHV-STM, Unisoku USM-1300S, equipped with an RHK R9 controller) [32]. To prevent oxidation, the STM measurements were performed after in situ cleaving of the sample under a vacuum of 10^{-6} mbar. Atomic force microscopy (AFM), conductive AFM (cAFM), and magnetic force microscopy (MFM) measurements were conducted using a Bruker Multimode 8 system with a thermal application controller (TAC) module to elevate the sample and tip temperature. Pt-coated tips were utilized for morphology measurement and electrical treatment. CoCr-coated tips were used for magnetic domain analysis [33,34]. Creation of bubble-like domains was localized using cAFM, employing either a constant voltage or a voltage cycle with alternated polarities under a perpendicular magnetic field.

Experimental results

The XRD and VSM data presented in Fig. 1 confirm the crystalline structure and magnetic properties of the Fe_3GaTe_2 single crystals. Fig. 1 (a) shows the atomic structure, validated by the XRD pattern in Fig. 1(b). The relative intensities and positions of the (00L) diffraction peaks align with previously reported results [11]. Notably, the (008) peak appears faint due to the structural factor. The inset provides an optical image of a representative flaky crystal, characterized by a 120° angle and a partially hexagonal morphology, features commonly observed in the hexagonal structures of 2D crystals [35].

The RT-ferromagnetism with PMA in Fe_3GaTe_2 was confirmed using VSM. Temperature-dependent zero-field-cooling (ZFC) and field-cooling (FC) magnetization measurements were conducted under a magnetic field of 1000 Oe, both in out-of-plane and in-plane configurations, as shown in Fig. 1(c). These measurements reveal a ferromagnetic transition with a Curie temperature (T_c) of approximately 367 K [11]. Magnetic hysteresis (M-H) loops were also measured for both configurations and are presented in Fig. 1(d) and (e), respectively. The out-of-plane M-H loop exhibited coercivities of approximately 200 Oe at 300 K and 1000 Oe at 2 K, while the in-plane loops demonstrated zero remanence and coercivity. Additionally, the saturation magnetic field in the in-plane geometry was found to be an order of magnitude larger than that in the out-of-plane geometry. These pronounced differences between the out-of-plane and in-plane M-H loops clearly indicate the presence of PMA in Fe_3GaTe_2 crystals [11,12,16].

The low-temperature STM measurement was conducted in UHV at 4–6 K, with the sample pre-cleaved at a load-lock chamber under 10^{-6} mbar to prevent oxidation. Fig. 2(a) shows the large-scale surface morphology of the Fe_3GaTe_2 bulk material under low-temperature STM. The atomic-resolved image confirms the single-crystalline structure and the Fourier transform image in Fig. 2(b) clearly exhibits the six-fold symmetry. Through the analysis of reciprocal lattice in Fig. 2(d), the lattice constant of Fe_3GaTe_2 is deduced as 4.01 ± 0.01 Å, closely matching the theoretical and experimental results from other studies [21]. In our wide-range and multi-area scan in a few micrometer scale, the sample surface appeared clean and atomically flat, with no observable step between terraces. This informs the standard characteristic of stable 2-dimensional structure after cleaving. Fig. 2(c) shows the magnified atomic structure, featuring the bright and repetitive triangular structures. As revealed in the top-view and cross-sessional atomic

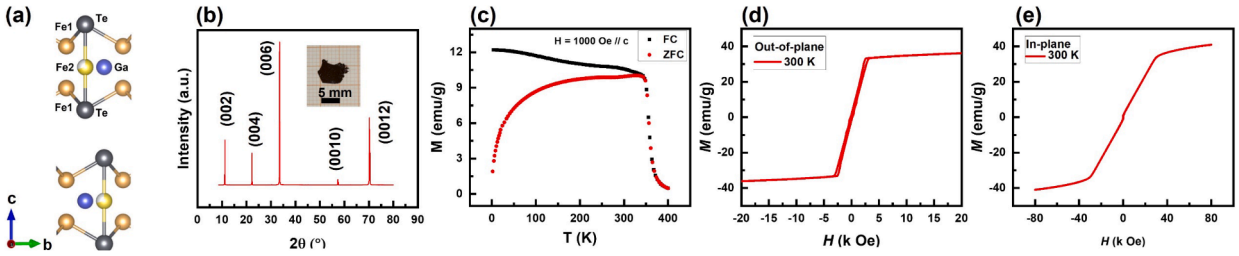

Fig. 1. (a) Schematic illustration of the layer-stacked Fe_3GaTe_2 crystalline structure. (b) XRD patterns and (c) temperature-dependent magnetic moment measurements under field-cooled (FC) and zero-field-cooled (ZFC) conditions for bulk Fe_3GaTe_2. (d) Out-of-plane and (e) in-plane magnetic hysteresis curves measured by VSM at RT.

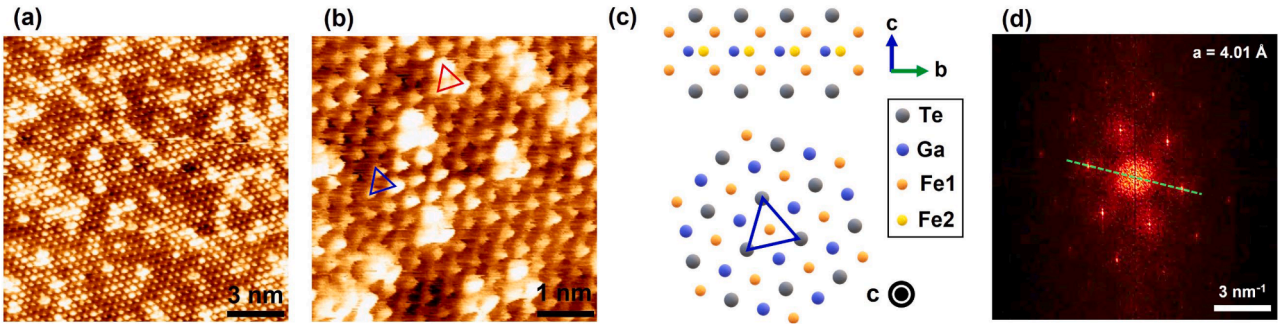

Fig. 2. (a) Atomically resolved low-temperature scanning tunneling microscopy (LT-STM) image of a cleaved Fe_3GaTe_2 crystal. The STM image was measured with a bias voltage of 0.6 V and a constant current of 200 pA. (b) Magnified STM image shows triangle features. (c) Schematic illustration showing the side and top views of the Fe_3GaTe_2 crystalline structure. (d) Fourier transform of the STM image in (a). From the indicated line profile, the lattice constant can be deduced.

structures of Fe_3GaTe_2 crystal, the Te atoms in the top layer correspond to the periodic hexagonal structure. The bright and repetitive triangles consist of three larger spots located in nearly the same position as the top Te atoms. Note that the height difference between the bright triangles and the background Te hexagons is much lower than an atomic height and should be attributed to local defects or irregularities in the underline layers, as created during the crystal growth. Supplementary Fig. S1 shows the STS results from a series of measurements across from the ordinary area (dark part) the triangle feature (bright part). A peak appears at around –0.1 V in dark part then shift to a peak at –0.3 V in bright part, as indicated by the arrows. This observation suggests the special electronic state in the triangle features. Based on the intensity analysis of the XRD peaks, Fe2 vacancy at the site nearby the Ga atom could exist. Liu et al.'s energy-dispersive X-ray spectroscopy analysis on Fe_3GaTe_2 also consistently indicates that the atomic ratio of Fe was slightly lower than 50 % [22]. In Li et al.'s report, their experimental study and DFT calculation found that the Fe deficiency in Fe_3GaTe_2 can lead to a pronounced displacement of the Fe atoms within the crystal structure, causing a structural transformation and resulting in a significant Dzyaloshinskii-Moriya interaction (DMI) [21]. The triangle features observed in STM images could be an indication of the presence of Fe-vacancy, which could change the electron distribution around nearby atoms, and accordingly affect STM signal of the top Te atoms, resulting in the triangle features on the surface.

Fig. 3 illustrates the evolution of the magnetic domain structure in Fe_3GaTe_2 as a function of the applied magnetic field. Consistent with the nearly zero remanence observed in Fig. 1(d), the domain structure at zero field comprises approximately equal proportions of bright and dark stripes. This pattern reflects the intrinsic PMA in Fe_3GaTe_2. In 2D-systems, such as thin films, a uniform out-of-plane magnetization is often unstable due to magnetic dipolar interaction. To minimize the overall energy, the system usually breaks into alternating stripe domains, where magnetization points up in one domain and down in the adjacent one. The periodicity of these stripe domains is influenced by factors such as film thickness, material composition, and external magnetic fields. Accordingly, magnetic stripe domains are a hallmark of materials with strong PMA, forming due to the interplay of anisotropy and dipolar interactions. Their controllability and tunability make them significant for emerging spintronic and memory applications.

The polar M-H loop in Fig. 1(d) shows a nearly constant slope up to saturation at 3000 Oe, indicating a gradual magnetization process. From a microscopic perspective, Fig. 3 reveals distinct mechanisms during magnetization reversal. As the magnetic field increases to 2000 Oe, the black domain stripes progressively narrow, while their overall shape, position, and structural characteristics remain largely unchanged. In the 2000–3000 Oe range, domain stripes begin to merge, with shorter branches particularly prone to coalescence. At fields around 4000 Oe, the domain contrast, as evidenced by the Kerr signal, diminishes until the magnetic domain structure disappears entirely. In contrast to conventional 3d transition metal films, where magnetization reversal is typically dominated by nucleation or domain wall motion at low and high fields [31,36], respectively, Fe_3GaTe_2 exhibits a distinct magnetization reversal behavior. This unique behavior is likely due to the non-neighboring Fe sites and the two-dimensional, layer-wise structure of Fe_3GaTe_2, which provide a specialized geometry for both intralayer and interlayer magnetic coupling [23].

As reported in previous studies, the field-cooling process from above the Curie temperature to RT under an appropriate perpendicular magnetic field can transform stripe domains into bubble domains [22,18]. To replicate this, we first demonstrate the formation of bubble domains across the entire Fe_3GaTe_2 sample by annealing it at 80 °C under a perpendicular magnetic field of ~200 Oe, applied using a heater-integrated sample holder. As shown in Supplementary Fig. S2, black bubble domains uniformly replace the original stripe domains upon cooling to RT. Notably, the application of a positive or negative perpendicular magnetic field during cooling results in white or black bubble domains, respectively, indicating that the spin orientation within the bubbles is dictated by the field direction. Furthermore, in our experiment, a cAFM was employed to apply a localized bias voltage and corresponding current to the Fe_3GaTe_2 sample through tip contact. The

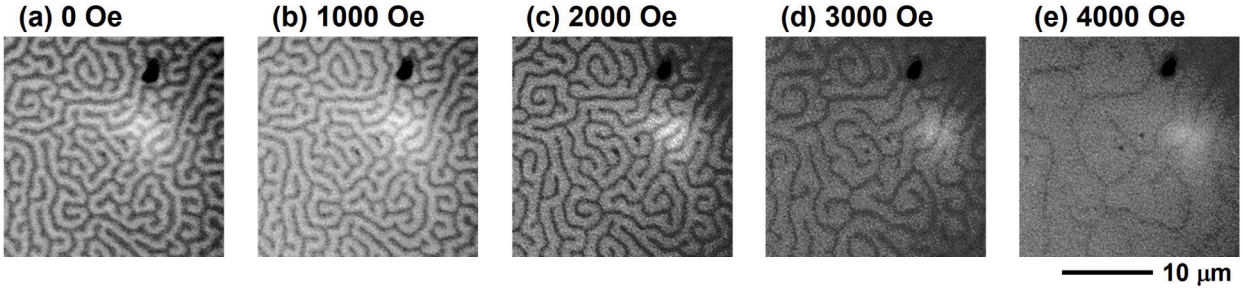

Fig. 3. Magnetic field-dependent domain evolution in a freshly cleaved Fe_3GaTe_2 crystal with a thickness of around 500 nm, captured using a magneto-optical Kerr microscope at RT.

contact area, estimated to be 100–200 nm, considers the tip size (20–30 nm) and surface deformation of both the Fe_3GaTe_2 and the tip under forced contact. This setup induces localized Joule heating in Fe_3GaTe_2, with an additional perpendicular magnetic field (~80 Oe) supplied by a permanent magnet beneath the sample holder. The effects of various parameters, including maximum current, application duration, and tip temperature, will be discussed in detail in the following sections.

Fig. 4 presents magnetic domain images captured by MFM after applying a constant bias of 10 V for durations of 2 and 8 min using cAFM. Under a perpendicular magnetic field of approximately 80 Oe, the domain structure within a circular region undergoes a significant transformation—from random stripe domains to bubble domains with radiating stripes. The effective circular area influenced by the bias expands from approximately 10 μm to 25 μm in diameter as the duration increases from 2 to 8 min. This effective area likely corresponds to the region where localized Joule heating raises the temperature above the T_c of Fe_3GaTe_2, facilitating the reorganization of the domain structure upon cooling. It is noteworthy that while the voltage and duration primarily affect the size of the effective area, the resulting bubble domains remain consistent in size regardless of these parameters.

Besides Fig. 4, another comparative study was conducted to clarify the potential influence of tip properties on the observed phenomena. Given that the effective circular area extends a few micrometers, the magnetic field contributed from the magnetic tip or the conducting electric current between the tip and sample is negligible. This conclusion is supported by a comparative experiment performed with a non-magnetic Pt-coated tip and a magnetic CoCr-coated tip, both of which yielded nearly identical results of triggering bubble domains. To confirm that localized Joule heating is the dominant factor, Fig. 5 demonstrates the creation of bubble domains under varying applied voltages. In this experiment, the voltage was cycled between positive and negative maximum values in monotonic steps over a 2-second duration. As shown in Fig. 5(b) and (d), reducing the maximum bias voltage from 10 V to 9 V decreased the effective area diameter from 6 μm to 4 μm. When the bias voltage was further reduced to 8 V, no observable changes in the pristine stripe domains were detected, as illustrated in Fig. 5(f). Considering that the contact between the cAFM tip and the sample surface behaves as a constant resistance, the heating power is expected to scale with the square of the applied bias voltage. Consequently, the size of the effective area is highly sensitive to the maximum voltage applied.

In Fig. 5, the applied voltage of 8 V appears to be close to the threshold voltage for SK formation. Since the primary mechanism is Joule heating induced by the applied voltage, which locally raises the sample temperature beyond T_c (350–380 K), several factors influence the threshold voltage, including the local thickness of the Fe_3GaTe_2 sample, contact area, contact resistance, and heating duration. For future spintronic applications, these parameters could be controlled by using nanoscale electrodes, enabling a more precise determination of the threshold voltage for bubble domain formation.

Fig. 6 illustrates the bubble domains (SKs) created in Fe_3GaTe_2 films of varying thickness using cAFM. Fig. 6 (a), (c), and (e) highlight

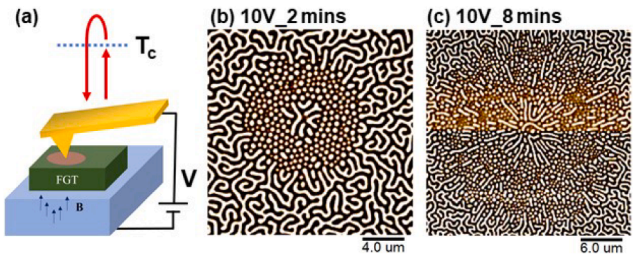

Fig. 4. (a) Schematic illustration of localized Joule heating using cAFM under a perpendicular magnetic field for the creation of bubble domains. (b), (c) MFM images taken after applying a 10 V bias voltage on a cleaved Fe_3GaTe_2 (~ 300 nm thick) surface for 2 min and 8 min, respectively, using cAFM.

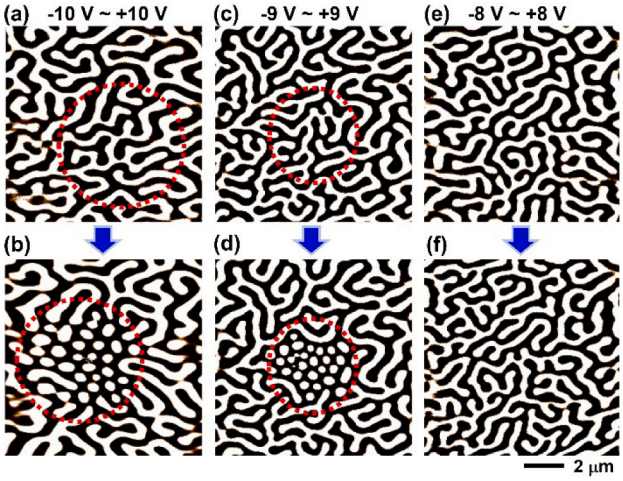

Fig. 5. MFM images measured on a 300 nm-thick Fe_3GaTe_2 flake show the domain structures before and after applying a cyclic bias voltage via cAFM, ranging from $-V_{max}$ to $+V_{max}$ and back to $-V_{max}$ in 2 s, under a perpendicular magnetic field. (a), (c), (e) Pristine domain structures. (b), (d) Dashed circles highlight newly formed bubble domains. (f) Stripe domains remain unchanged compared to (e). All MFM images have a size of 10 × 10 μm^2.

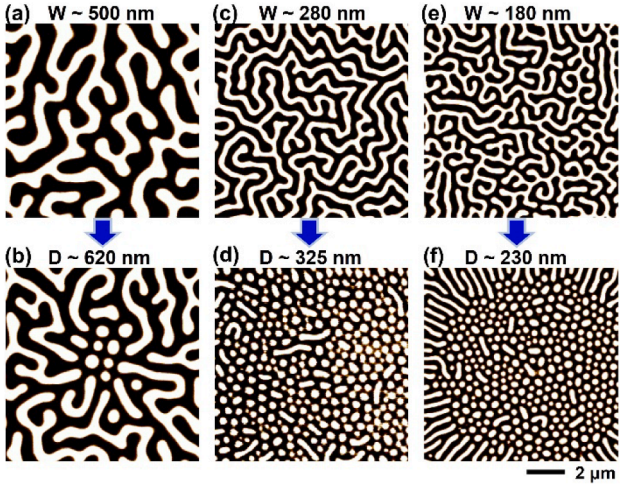

Fig. 6. MFM images showing domain structures before and after applying a constant 10 V bias voltage for 4 min via cAFM under a perpendicular magnetic field. (a), (c), (e) Pristine domain structures of Fe_3GaTe_2 samples with varying thicknesses, showing different stripe widths (W). (b), (d), (f) Bubble domains induced by cAFM, with average diameters (D) indicated. All MFM images have a size of 10 × 10 μm^2.

samples with distinct average stripe widths of 500 nm, 280 nm, and 180 nm, respectively. According to the previous experimental results [22], the stripe domain width is monotonically correlated with the thickness of Fe_3GaTe_2. Based on the statistical data, the samples with these stripe widths correspond to Fe_3GaTe_2 thicknesses of approximately 1 μm, 200 nm, and 100 nm, respectively [22]. The diameters of the resulting bubble domains in these samples were measured as 620 ± 100 nm, 325 ± 80 nm, and 230 ± 70 nm, respectively. These results reveal a wide size distribution, with bubble diameters varying by ±20–30 % around the mean. Additionally, the bubble domain diameters were approximately 20 ± 5 % larger than the pristine stripe widths, suggesting a consistent scaling relationship, as shown in the statistical analysis in Fig. 7. This similarity in domain size and distribution implies that the same underlying physical mechanisms govern both stripe and bubble domain structures. These mechanisms likely include magnetostatic energy,

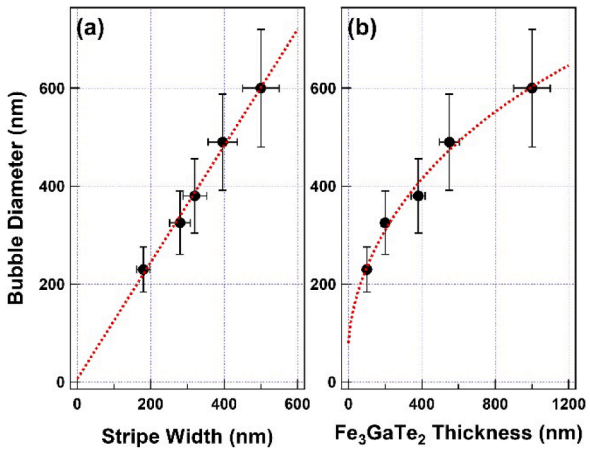

Fig. 7. Statistical analysis of the cAFM-created bubble domain diameters (D): (a) Comparison between D and the width of pristine stripe domains, and (b) Dependence of D on the thickness of Fe_3GaTe_2. The dashed line in (a) and the curve in (b) are guides to the eye.

domain wall energy, and potential contributions from the DMI.

Following the successful demonstration of localized creation of bubble domains, the next question is how to maximize the effective area of bubble domain generation using cAFM. Intuitively, increasing the bias voltage should expand the effective area. However, higher bias voltages or currents risk causing defects at the contact point due to oxidation and potential mechanical damage from elevated temperatures. To mitigate this, employing a cAFM tip with an elevated temperature offers a promising alternative for enlarging the effective area. Fig. 8 illustrates bubble domains generated using a tip heated to 200 °C. In this experiment, SKs were created by scanning a 5 × 5 μm area of the Fe_3GaTe_2 surface with a bias voltage of 10 V for 4 min. The enhanced contact facilitated heat transfer from the heated tip, effectively raising the local base temperature of Fe_3GaTe_2. As a result, the effective area expanded significantly, reaching a diameter of nearly 40 μm. It is noteworthy that using only a heated tip at 200 °C, without applied bias, failed to generate bubble domains. This suggests that the heat transfer rate through the tip alone is insufficient to elevate the local Fe_3GaTe_2 temperature above the threshold required for bubble domain formation. Joule heating induced by the applied voltage/current remains more efficient in local heating. However, pre-heating the sample with a heated

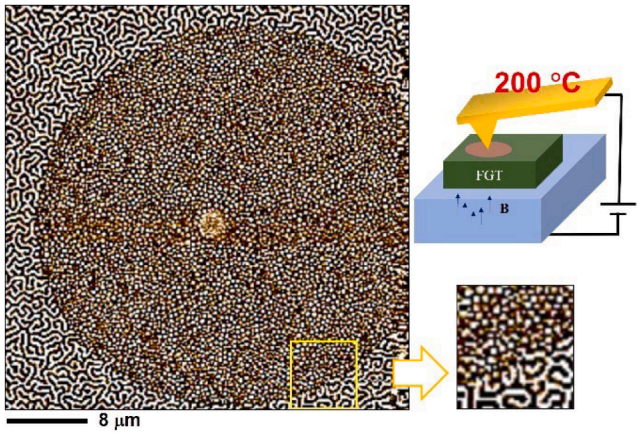

Fig. 8. MFM image of bubble domains created via cAFM at an elevated tip temperature of 200 °C, under a perpendicular magnetic field. The bubble domains were generated by scanning a 5 × 5 μm^2 area on the Fe_3GaTe_2 surface with a 10 V bias for 4 min. The image size is 40 × 40 μm^2. The inset includes a schematic of the experimental setup and a magnified MFM image at the boundary of the affected region.

tip could reduce the critical voltage/current required for SK formation, minimizing the risk of damage to the Fe_3GaTe_2 surface at the contact point.

Following the experiment of Fig. 8, we did attempt to explore the threshold temperature for inducing bubble domains without applying an external bias; however, several factors can seriously influence the heating results, such as the local thickness of Fe_3GaTe_2 and the size of the contact area, which depends on the tip shape and the applied normal force. In the method using a heated tip without an external bias, the temperature elevation of Fe_3GaTe_2 primarily depends on heat transfer from the tip. Consequently, the competition between lateral and depth-wise heat dissipation rates becomes a crucial factor, which strongly depends on the local thickness of Fe_3GaTe_2. Additionally, upon contacting the sample, the tip temperature is expected to drop abruptly, making the balance between tip heating power and sample heat dissipation rate a critical aspect of the heating process. Given these complexities, our study focuses on applied voltage-induced Joule heating, which is more efficient in terms of heating power, speed, and localization.

Discussion

In general, cAFM is primarily used to detect surface conductance. For instance, in our previous study on cobalt-oxide nanocluster formation, cAFM was employed to microscopically investigate surface conductivity [33]. The topographic and current images exhibited a strong correlation, confirming the insulating nature of the nanoclusters [33]. Recently, cAFM with a spin-polarized tip has been widely used to detect spin-dependent conductivity in novel materials, such as chiral perovskites [37]. Additionally, an ultrahigh-resolution probe technique for characterizing the nanoscale Seebeck coefficient has been developed using a modified cAFM probe with local heating functionality [38]. The heated cAFM tip enables nanoscale thermal contact with thermoelectric samples, successfully generating a localized thermoelectric signal [38]. To the best of our knowledge, our experiment is the first demonstration of bubble domain creation via cAFM, achieved through Joule heating induced by an applied voltage. Fig. 6(b) demonstrates the creation of a few bubbles within areas smaller than 5 μm^2, while Figs. 5(d) and 9(d) show similar localized formations in areas of approximately 10 μm^2. In contrast, Fig. 8 illustrates large-area bubble domain formation, with up to nearly 10^4 bubbles within a 1200 μm^2 region.

Since the primary mechanism is Joule heating induced by the applied voltage, which locally raises the sample temperature beyond T_c (350–380 K), conductive tips other than Pt-coated ones should also produce similar results. Additionally, suppose the tip is coated with a magnetic metallic layer that generates a perpendicular magnetic field. In that case, the cAFM can simultaneously heat the local area of Fe_3GaTe_2 while applying an external magnetic field, both of which are sufficient for the creation of bubble domains. In this case, an external magnet beneath the sample holder would no longer be necessary to provide the perpendicular field.

In Figs. 4 and 6, in addition to the bubble domains, radiative stripe domains are observed either at the center or in the surrounding regions of the effective area. The formation of these radiative stripes may be attributed to the influence of electric current, temperature gradients, or electric fields within the effective zone. Supplementary Fig. S3 presents a comparative experiment conducted during the creation of SKs via uniform field cooling, where a cAFM tip applies voltage along a specified trajectory. Importantly, the tip was positioned close to the sample surface without establishing direct electrical contact, ensuring no measurable conduction current was present. As shown in Supplementary Fig. S3, no radiative stripe domains appear along the tip trajectory; the surface predominantly consists of bubble domains. This observation excludes the possibility of a surface-normal electric field between the tip and sample being responsible for the stripe domains. However, during voltage application via the cAFM tip, the electric field and current

distribution radiate outward from the contact point. Similarly, the temperature gradient is expected to exhibit a comparable radiative distribution. Previous studies provide possible mechanisms related to these phenomena. For instance, Ba et al. demonstrated skyrmion manipulation through strain-mediated magnetoelectric coupling via electric fields [39]. Chiba et al. showed that applying an electric field could alter the velocity of magnetic domain walls by more than an order of magnitude, attributed to electrical modulation of the energy barrier for domain wall motion [40]. These findings suggest that the radiative stripe domains observed in this study could be driven by the radiative distribution of the electric field or by strain distribution induced by temperature gradients.

Given the complexity of the system, where the multiple mechanisms mentioned above likely act simultaneously, isolating the contribution of each factor remains challenging. Further experimental investigations are necessary to identify the dominant mechanism definitively. Nevertheless, as shown in Fig. 8, when bubble domains are created using a heated tip, only bubble domains are present. This suggests that with an elevated local base temperature, the influence of mechanisms responsible for radiative stripes could be significantly reduced. Fig. 9 presents comparative experiments exploring the impact of variable temperatures on Fe_3GaTe_2. At RT, applied voltages of 5 V and 7 V were insufficient to induce the formation of bubble domains. However, as shown in Fig. 9(c), applying 10 V to the RT sample using cAFM for 4 min resulted in a large area of SK bubbles, some of which formed elongated domains. A notable defect, observed as a blurry spot at the center of the image, marks the tip-sample contact point. This voltage-dependent behavior aligns with the findings in Fig. 5, where a cyclic voltage was applied for 2 s.

In contrast, Fig. 9(d) demonstrates that at an elevated sample temperature of 55 °C, a lower voltage of 7 V can successfully generate bubble domains over an area of approximately 20 μm^2. This suggests that when Fe_3GaTe_2 is heated to a temperature close to but below its T_c, the additional heat provided by the cAFM tip serves as a critical trigger. Consequently, the required voltage for bubble formation, along with the potential for defect creation at the tip-sample interface and other electric field or current effects, is significantly reduced. Notably, since the background temperature of Fe_3GaTe_2 remains below T_c, the domain structures outside the cAFM-affected area remain unchanged.

Previous studies have shown that the transition from stripe to bubble domains depends on perpendicular field cooling through the transition temperature T_c. Therefore, two strategies are feasible to achieve localized creation of bubble domains: applying a localized magnetic field while maintaining uniform heating or inducing localized heating under a uniform magnetic field. For example, in the study by Jin et al., an MFM tip was used to provide a localized magnetic field, while uniform temperature control was maintained through the sample holder [41]. However, in this approach, both the magnitude and direction of the stray field from the magnetic tip can vary depending on its relative position to the sample. Additionally, the process requires the entire domain structure to be reset by heating the sample above T_c each time the bubble domains are created. In contrast, our study employs a more efficient method. By maintaining a localized perpendicular field of approximately 80–100 Oe, pristine domains remain unaffected, and localized bubble domains can be generated via Joule heating induced by a nanoscale contact through a cAFM tip. As illustrated in Supplementary Fig. S4, bubble domains were successfully triggered at two separate contact points, 30 μm apart, for domain overlap analysis. Each triggered region formed SKs within a circular area surrounded by radiative stripe domains. Importantly, when the second trigger was applied, new bubble domains were created in the overlapping area, effectively overwriting the pre-existing domains. This demonstrates the re-writability of the domain structure. Notably, the regions outside the overlap in the initially triggered area remained unchanged, confirming the localized nature of the bubble domain creation process.

For the cAFM-induced nucleation of bubble domains, with the applied normal force fixed at 150 nN, the voltage and duration time vary as specified in each experiment. Based on our previous study on the AFM tip scanning effect on graphene (Gr)/MoS_2, a tip normal force above 200 nN can break Gr on MoS_2 [34]. To prevent tip-induced mechanical damage to the 2D Fe_3GaTe_2 material, we carefully selected the contact force for the cAFM experiments. Controlling the electric current between the cAFM tip and the Fe_3GaTe_2 sample is challenging due to intense heating effects, which can create a steep temperature gradient and cause mechanical instability. The I/V curve occasionally shows abrupt current changes. The built-in current meter has a maximum scale of 1 μA, but the actual current is likely much higher.

In the above demonstrative experiments, several uncertainties still limit the reproducibility of the proposed method. For instance, although localized bubble domain creation using cAFM was performed in a low-humidity environment (<10 %) with continuous nitrogen gas flow to minimize the sample degradation, the possibility of electrochemical reactions and oxidation near the contact area cannot be entirely ruled out. Furthermore, despite feedback control to maintain a constant normal force, the application of electric current results in significant heating of both the tip and the sample surface. This intense heating can create a steep temperature gradient, potentially causing mechanical instability, such as uneven contact or rotational torque on the tip. These factors introduce uncertainties in the local Joule heating process, particularly since the heating power (P) is determined by $P=V^2/R$ under constant voltage (V) conditions, where R is the contact resistance. Variations in resistance due to mechanical or electrochemical effects further contribute to instability. For future applications in spintronics, these uncertainties could be mitigated by using nano-sized electrodes with protective coating layers [14]. This geometry would enable localized heating for bubble domain creation while preventing issues such as oxidation and mechanical instability, thereby improving reliability and precision.

This cAFM-heating method should be highly dependent on several

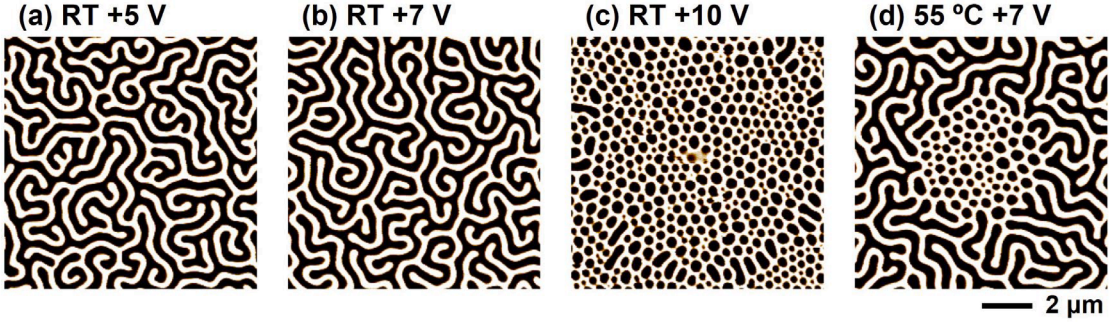

Fig. 9. MFM images taken after applying a constant voltage of (a) 5 V, (b) 7 V, and (c) 10 V for 4 min by CAFM under a perpendicular magnetic field while the Fe_3GaTe_2 sample is at room temperature (RT). (d) The MFM image was taken after applying a constant voltage of 7 V for 4 min while the sample is uniformly heated to an elevated temperature of 55 °C.

critical parameters, including the contact area, the thermal capacity of the crystal, and the thermal coupling to the sample holder. Since this method relies on localized heating via tip-sample contact resistance, extensive heat transfer is not expected. A high current density applied over a sufficiently short duration should effectively heat the contact area while minimizing heat dissipation, enabling the localized creation of bubble domains. Under the chosen parameters in this study, bubble domains were generated with high reproducibility, achieving a success rate of over 70 %. As shown in Fig. 9, when the sample temperature is raised to 55 °C, the success rate increases further, reaching nearly 100 %, as the cAFM heating only needs to provide the final energy boost for bubble domain formation.

The reversibility and reproducibility of bubble domain creation and annihilation are crucial for practical device applications. Although not yet demonstrated, removing the perpendicular magnetic field and applying localized re-heating above T_c using cAFM could potentially annihilate the bubble domains and restore the pristine stripe domains. This possibility presents an intriguing avenue for future research.

Conclusion

This study provides a detailed investigation into the localized creation of SKs using cAFM under an applied magnetic field. By adjusting key experimental parameters, such as bias voltage, tip temperature, and application duration, the density and size of the resulting bubble domains could be finely tuned, demonstrating a scalable approach to bubble domain generation with controlled dimensions. The results show that the induced bubble domains exhibit a consistent scaling relationship with the thickness of the Fe_3GaTe_2 layer. Additionally, the study highlights the re-writability of the domain structure and the importance of localized heating via Joule heating for efficient bubble domain creation. The observed stability issues related to contact points can be addressed by employing nano-sized electrodes with protective coatings, paving the way for more reliable and efficient fabrication of skyrmion-based devices in future applications.

CRediT authorship contribution statement

Chak-Ming Liu: Writing – original draft, Investigation, Conceptualization. **Yi-Jia Liu:** Writing – original draft, Methodology, Investigation, Data curation, Conceptualization. **Po-Chun Chang:** Writing – original draft, Methodology, Investigation, Conceptualization. **Po-Wei Chen:** Investigation, Data curation. **Masahiro Haze:** Investigation, Data curation. **Ming-Hsien Hsu:** Investigation, Data curation. **Neleena Nair Gopakumar:** Investigation. **Yishui Zhou:** Methodology. **Yung-Hsiang Tung:** Methodology. **Sabreen Hammouda:** Methodology. **Chao-Hung Du:** Visualization, Resources, Project administration. **Yukio Hasegawa:** Methodology, Investigation, Data curation. **Yixi Su:** Resources, Project administration, Methodology, Investigation. **Hsiang-Chih Chiu:** Writing – review & editing, Visualization, Supervision, Resources, Investigation, Conceptualization. **Wen-Chin Lin:** Conceptualization, Data curation, Formal analysis, Funding acquisition, Investigation, Project administration, Resources, Supervision, Validation, Visualization, Writing – original draft, Writing – review & editing.

Declaration of competing interest

The authors declare the following financial interests/personal relationships which may be considered as potential competing interests:

Wen-Chin Lin reports financial support was provided by National Science and Technology Council. If there are other authors, they declare that they have no known competing financial interests or personal relationships that could have appeared to influence the work reported in this paper.

Acknowledgments

The authors thank the Physics Lab of Heinz Maier-Leibnitz Zentrum (MLZ) for the operational support in the physical property measurements. This study was financially sponsored by the National Science and Technology Council of Taiwan under grant no NSTC 111-2923-M-003-001-MY3, NSTC 112-2112-M-003-011, NSTC 113-2811-M-032-002, NSTC 113-2112-M-003-004, NSTC 113-2811-M-032-002, and NSTC 113-2112-M-003-012.

Supplementary materials

Supplementary material associated with this article can be found, in the online version, at doi:10.1016/j.apsadv.2025.100718.

Data availability

Data will be made available on request.

References

[1] C. Gong, L. Li, Z. Li, H. Ji, A. Stern, Y. Xia, T. Cao, W. Bao, C. Wang, Y. Wang, Z. Q. Qiu, R.J. Cava, S.G. Louie, J. Xia, X. Zhang, Nature 546 (2017) 265–269.
[2] M. Gibertini, M. Koperski, A.F. Morpurgo, K.S. Novoselov, Nat. Nanotech. 14 (2019) 408–419.
[3] G.-H. Lee, Y.J. Yu, X. Cui, N. Petrone, C.-H. Lee, M.S. Choi, D.-Y. Lee, C. Lee, W. J. Yoo, K. Watanabe, T. Taniguchi, C. Nuckolls, P. Kim, J. Hone, ACS Nano 7 (2013) 7931–7936.
[4] Y. Yu, T. Minhaj, L. Huang, Y. Yu, L. Cao, Phys. Rev. Appl. 13 (2020) 034059.
[5] S. Ghosh, W. Bao, D.L. Nika, S. Subrina, E.P. Pokatilov, C.N. Lau, A.A. Balandin, Nat. Mater. 9 (2010) 555–558.
[6] M. Gibertini, M. Koperski, A.F. Morpurgo, K.S. Novoselov, Nat. Nanotech. 14 (2019) 408–419.
[7] C.-T. Kuo, M. Neumann, K. Balamurugan, H.J. Park, S. Kang, H.W. Shiu, J.H. Kang, B.H. Hong, M. Han, T.W. Noh, J.-G. Park, Sci. Rep. 6 (2016) 20904.
[8] K.-zhao Du, X.-zhi Wang, Y. Liu, P. Hu, M. Iqbal Bakti Utama, C.K. Gan, Q. Xiong, C. Kloc, ACS Nano 10 (2016) 1738–1743.
[9] B. Huang, G. Clark, E. Navarro-Moratalla, D.R. Klein, R. Cheng, K.L. Seyler, D. Zhong, E. Schmidgall, M.A. McGuire, D.H. Cobden, W. Yao, X. Di, P. Jarillo-Herrero, X. Xu, Nature 546 (2017) 270–273.
[10] B. Ding, Z. Li, G. Xu, H. Li, Z. Hou, E. Liu, X. Xi, F. Xu, Y. Yao, W. Wang, Nano Lett. 20 (2020) 868–873.
[11] G. Zhang, F. Guo, H. Wu, X. Wen, L. Yang, W. Jin, W. Zhang, H. Chang, Nat. Commun. 13 (2022) 5067.
[12] A.M. Ruiz, D.L. Esteras, D. López-Alcalá, J.J. Baldoví, Nano Lett. 24 (2024) 7886–7894.
[13] W. Jin, G. Zhang, H. Wu, L. Yang, W. Zhang, H. Chang, Nanoscale 15 (2023) 5371.
[14] W. Jin, G. Zhang, H. Wu, L. Yang, W. Zhang, H. Chang, ACS Appl. Mater. Interface. 15 (2023) 36519–36526.
[15] H. Pan, C. Zhang, J. Shi, X. Hu, N. Wang, L. An, R. Duan, P. Deb, Z. Liu, W. Gao, ACS Mater. Lett. 5 (2023) 2226.
[16] H. Algaidi, C. Zhang, Y. Ma, C. Liu, A. Chen, D. Zheng, X. Zhang, APL Mater. 12, 011124 (2024).
[17] G. Hu, H. Guo, S. Lv, L. Li, Y. Wang, Y. Han, L. Pan, Y. Xie, W. Yu, K. Zhu, Q. Qi, G. Xian, S. Zhu, J. Shi, L. Bao, X. Lin, W. Zhou, H. Yang, H.-jun Gao, Adv. Mater. 36 (2024) 2403154.
[18] Y. Ji, S. Yang, H.-B. Ahn, K.-W. Moon, T.-S. Ju, M.-Y. Im, H.-S. Han, J. Lee, S.-y. Park, C. Lee, K.-J. Kim, C. Hwang, Adv. Mater. 36 (2024) 2312013.
[19] S. Liu, S. Hu, X. Cui, T. Kimura, Adv. Mater. 36 (2024) 2309776.
[20] G. Zhang, J. Yu, H. Wu, L. Yang, W. Jin, W. Zhang, H. Chang, Appl. Phys. Lett. 123 (2023) 101901.
[21] Z. Li, H. Zhang, G. Li, J. Guo, Q. Wang, Y. Deng, Y. Hu, X. Hu, C. Liu, M. Qin, X. Shen, R. Yu, X. Gao, Y. Zhu, Z. Liao, J. Liu, Z. Hou, X. Fu, Nat. Commun. 15 (2024) 1017.
[22] H. Zhang, D. Raftrey, Y.-T. Chan, Y.-T. Shao, R. Chen, X. Chen, X. Huang, J. T. Reichanadter, K. Dong, S. Susarla, L. Caretta, Z. Chen, J. Yao, P. Fischer, J. B. Neaton, W. Wu, D.A. Muller, R.J. Birgeneau, R. Ramesh, Sci. Adv. 8 (2022) eabm7103.
[23] R. Iimori, S. Hu, A. Mitsuda, T. Kimura, Commun. Mater. 5 (2024) 235.
[24] C. Liu, S. Zhang, H. Hao, H. Algaidi, Y. Ma, X.-X. Zhang, Adv. Mater. 36 (2024) 2311022.
[25] X. Hou, H. Wang, B. Zhang, C. Xu, L. Sun, Z. Li, X. Wang, K. Qu, Y. Wei, Y. Guo, Appl. Phys. Lett 124 (2024) 142404.
[26] W.J. Heinonen, H. Somaily, S.G.E.te Velthuis, A. Hoffmann, Phys. Rev. B 93 (2016) 094407.
[27] W. Jiang, P. Upadhyaya, W. Zhang, G. Yu, M. Benjamin Jungfleisch, F.Y. Fradin, J. E. Pearson, Y. Tserkovnyak, K.L. Wang, O. Heinonen, S.G.E. te Velthuis, A. Hoffmann, Science 349 (2015) 283.
[28] M. Schott, A. Bernand-Mantel, L. Ranno, S. Pizzini, J. Vogel, H. Bea, C. Baraduc, S. Auffret, G. Gaudin, D. Givord, Nano Lett. 17 (2017) 3006–3012.

[29] S.-G. Je, P. Vallobra, T. Srivastava, J.-C. Rojas-Sanchez, T.H. Pham, M. Hehn, G. Malinowski, C. Baraduc, S. Auffret, G. Gaudin, S. Mangin, H. Bea, O. Boulle, Nano Lett. 18 (2018) 7362–7371.
[30] P.-C. Chang, Y.-Y. Chang, W.-H. Wang, F.-Y. Lo, W.-C. Lin, Commun. Chem. 2 (2019) 89.
[31] W.-H. Wang, C.-Y. Pan, C.-M. Liu, W.-C. Lin, P.-hsun Jiang, ACS Appl. Mater. Interface. 14 (2022) 20151–20158.
[32] H.-H. Yang, C.C. Hsu, W.-C. Lin, Y. Hasegawa, Phys. Rev. B 104 (2021) 035422.
[33] C.-C. Hsu, H.-C. Chiu, Y.-C. Chen, P.-C. Chang, C.-T. Wu, H.-W. Yen, W.-C. Lin, Appl. Surf. Sci. 416 (2017) 133–143.
[34] C.-M. Liu, W.-H. Chang, E.-D. Chu, C.-H. Yin, Y.-W. Lan, H.-C. Chiu, W.-C. Lin, Appl. Surf. Sci. 644 (2024) 158778.
[35] Y. Zhang, J. Chu, L. Yin, T.A. Shifa, Z. Cheng, R. Cheng, F. Wang, Y. Wen, X. Zhan, Z. Wang, J. He, Adv. Mater. 31 (2019) 1900056.
[36] P.-C. Chang, C.-M. Liu, C.-C. Hsu, W.-C. Lin, Sci. Rep. 8 (2018) 6656.
[37] Y. Lu, Q. Wang, R. Chen, L. Qiao, F. Zhou, X. Yang, D. Wang, H. Cao, W. He, F. Pan, Z. Yang, C. Song, Adv. Funct. Mater. 31 (2021) 2104605.
[38] K.Q. Xu, H.R. Zeng, H.Z. Yu, K.Y. Zhao, G.R. Li, J.Q. Song, X. Shi, L.D. Chen, Appl. Phys. A 118 (2015) 57–61.
[39] Y. Ba, S. Zhuang, Y. Zhang, Y. Wang, Y. Gao, H. Zhou, M. Chen, W. Sun, Q. Liu, G. Chai, J. Ma, W. Jiang, C. Nan, J.-M. Hu, Y. Zhang, Y. Zhao, H. Tian, H. Du, Nat. Commun. 12 (2021) 322.
[40] D. Chiba, M. Kawaguchi, S. Fukami, N. Ishiwata, K. Shimamura, K. Kobayashi, T. Ono, Nat. Commun. 3 (2012) 888.
[41] S. Jin, Z. Wang, S. Dong, Y. Wang, K. Han, G. Wang, Z. Deng, X. Jiang, Y. Zhang, H. Huang, J. Hong, X. Wang, T. Xia, S.-W. Cheong, X. Wang, J. Materiom. 11 (2025) 100865.